ACS OMEGA

Article

http://pubs.acs.org/journal/acsodf

Photoluminescence Blinking of Single-Crystal Methylammonium Lead Iodide Perovskite Nanorods Induced by Surface Traps

Haifeng Yuan,*[,†] Elke Debroye,[†] Giorgio Caliandro,[†] Kris P. F. Janssen,[†] Jordi van Loon,[‡] Christine E. A. Kirschhock,[‡] Johan A. Martens,[‡] Johan Hofkens,[†,§] and Maarten B. J. Roeffaers*[,‡]

[†]Department of Chemistry, KU Leuven, Celestijnenlaan 200F, B-3001 Leuven, Belgium

[‡]Centre for Surface Chemistry and Catalysis, KU Leuven, Kasteelpark Arenberg 23, 3001 Heverlee, Belgium

[§]RIES, Hokkaido University, N20W10, Kita-Ward, Sapporo 001-0020, Japan

Supporting Information

ABSTRACT: Photoluminescence (PL) of organometal halide perovskite materials reflects the charge dynamics inside of the material and thus contains important information for understanding the electro-optical properties of the material. Interpretation of PL blinking of methylammonium lead iodide ($MAPbI_3$) nanostructures observed on polycrystalline samples remains puzzling owing to their intrinsic disordered nature. Here, we report a novel method for the synthesis of high-quality single-crystal $MAPbI_3$ nanorods and demonstrate a single-crystal study on $MAPbI_3$ PL blinking. At low excitation power densities, two-state blinking was found on individual nanorods with dimensions of several hundred nanometers. A super-resolution localization study on the blinking of individual nanorods showed that single crystals of several hundred nanometers emit and blink as a whole, without showing changes in the localization center over the crystal. Moreover, both the blinking ON and OFF times showed power-law distributions, indicating trapping−detrapping processes. This is further supported by the PL decay times of the individual nanorods, which were found to correlate with the ON/OFF states. Furthermore, a strong environmental dependence of the nanorod PL blinking was revealed by comparing the measurements in vacuum, nitrogen, and air, implying that traps locate close to crystal surfaces. We explain our observations by proposing surface charge traps that are likely related to under-coordinated lead ions and methylammonium vacancies to result in the PL blinking observed here.

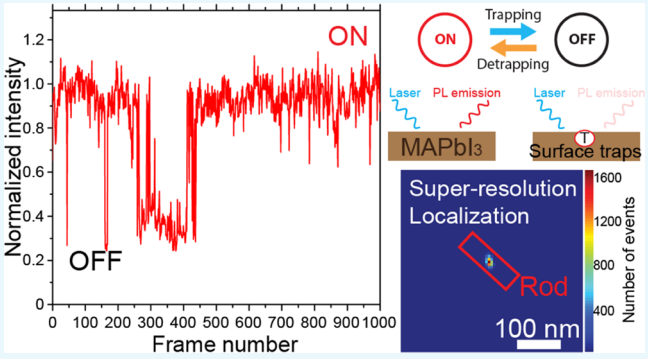

INTRODUCTION

Reporting power-conversion efficiencies exceeding 20%,[1,2] the recent emergence of organometal halide perovskites (OHPs), methylammonium lead iodide ($MAPbI_3$) in particular, has enabled new possibilities for cost-efficient photovoltaic (PV) devices.[3,4] OHP properties such as photoluminescence (PL), charge mobility, trap density, and their PV performance, however, are found to vary largely depending on the material preparation and processing methods,[5] likely due to differences in the defect density and crystal morphology. The conventionally employed deposition method for OHP solar-cell fabrication is by annealing a spin-casted precursor film at elevated temperatures,[6,7] resulting in a polycrystalline film composed of densely packed crystal grains of a few hundred nanometers up to micrometers in size. The crystal grains in the film show large variations in their size and morphology. PL and cathodoluminescence from such OHP films, reflecting local charge dynamics,[8−12] have recently been shown to be highly heterogeneous from grain to grain.[6,13,14] Moreover, a recent study using simultaneous light and electron microscopy has revealed significant variations in both PL and morphology evolution of perovskite crystals upon light- and electron-beam-induced degradation.[15] The aforementioned heterogeneity found in submicron-sized perovskites is closely related to variations in the local ion mobility,[13,15−18] trap densities,[19] and local chemical composition,[6,13,16,20] which ultimately determine the device performance on mesoscopic and macroscopic scales.[17,18,21−23] Besides OHP crystals themselves, the inherent grain boundaries in the polycrystalline films are also found to play an important role in the properties of OHP-based devices.[24,25]

To best resolve such heterogeneity in the crystal properties and the role of grain boundaries, the link between morphology and material properties needs to be established at the single-crystal level. Applying super-resolution localization microscopy on individual particles on a glass cover slide prepared using the conventional film deposition method, Tian et al. reported on light-activated quenching sites in single perovskite particles that

Received: July 6, 2016
Accepted: July 14, 2016
Published: July 26, 2016

DOI: 10.1021/acsomega.6b00107
ACS Omega 2016, 1, 148−159

cause giant PL blinking.[7] Super-resolution localization on these blinking events revealed that the localization center position was jumping for the sub-diffraction-limit nanocrystals studied.[7] Furthermore, the authors reported a strong correlation between PL intensities and the corresponding localization center positions.[7] Whereas these data represent a first-of-its-kind report on OHP nanocrystal PL blinking, studies correlating optical localization with morphology at the nanometer scale are still missing, leaving the mechanism behind the PL blinking phenomenon elusive. In particular, the sample preparation method employed in the previous study by Tian et al.[7] cannot exclude the existence of multiple crystal grains within a diffraction-limited spot. Therefore, single-crystalline OHP nanocrystals, nanorods in particular, are required to minimize the effects caused by polycrystallinity in the aforementioned super-resolution optical studies.

Although a few studies have reported on the solution synthesis of single-crystal OHP nanostructures,[26,27] such as quantum dots,[28] rod- and wire-type crystals,[29−32] and platelets,[33] controlled synthesis of OHP rods (100−300 nm) remains challenging. The surface-initiated solution growth of a single-crystalline OHP gives well-isolated OHP wires and plates of high quality.[29,30] However, this method requires an initial step that uses a solid surface and results in crystals of a few microns in size.[29,30] A total solution-based synthesis of OHP nanorods (an average dimension of 800 × 50 nm^2) was recently demonstrated by Zhu et al. by employing *n*-octylammonium cations as capping agents.[31] Nevertheless, these nanorods (800 nm in length) are much longer than the diffraction limit of visible light (200−300 nm). This makes them not ideal for super-resolution localization studies in which 2D Gaussian is usually used to approximate the point-spread function (PSF) of single emitters.[34,35] Very recently, Aharon et al. used octylammonium iodide and oleic acid (OA) to control the OHP nanocrystal morphology and reported on high-yield synthesis of OHP nanorods of 11 × 2 nm^2.[32] Such crystals are too small to draw useful conclusions from the super-resolution localization studies because the resolution of this imaging modality is only several tens of nanometers[34−36] and spatial-related PL phenomena on the sub-10 nm length scale are out of reach.

In this study, we first present a novel method to synthesize single-crystalline $MAPbI_3$ nanorods with an average dimension of 160 × 35 nm^2, using a combination of oleylamine (OAm) and OA as capping agents. It is noteworthy that the resulting $MAPbI_3$ nanorods are exceptionally stable in toluene suspension even after 8 weeks of storage in the dark. Next, we investigate the PL blinking of the as-prepared individual $MAPbI_3$ nanorods using correlative super-resolution localization optical microscopy and scanning electron microscopy (SEM).[15] Finally, we discuss our experimental observations by proposing under-coordinated lead ions and methylammonium vacancies to be the surface traps that lead to PL blinking of $MAPbI_3$ nanorods observed in this study.

RESULTS AND DISCUSSION

$MAPbI_3$ Nanorods. $MAPbI_3$ nanorods were prepared via a two-step synthesis. The capping agents, OAm and OA, were first dissolved in toluene. On injecting the precursor acetonitrile solution into the capping agent toluene solution under vigorous stirring, tiny $MAPbI_3$ nuclei started to form, resulting in a color change of the suspension to red. Further crystal growth was achieved by gradually introducing additional amounts of pure toluene into the mixture to drive further precipitation of $MAPbI_3$ precursors. A detailed description of the synthesis method can be found in Experimental Section.

The concentration ratio between the two capping agents is crucial for the anisotropic growth of $MAPbI_3$ nanocrystals. On the one hand, when OA was used as the only capping agent, the $MAPbI_3$ nanocrystals grown consisted mostly of large bulky clusters of small nanoparticles. On the other hand, elongated thin wires were found when OAm was used as the only capping agent. However, $MAPbI_3$ nanocrystals are found to be stable only in the presence of OA. In the absence of OA, the nanowires quickly aggregate within several hours of stirring during synthesis, leading to a clear and transparent suspension. The anisotropic growth of nanorods is likely due to the complex dynamic binding of OAm and OA onto certain crystal facets of $MAPbI_3$ during crystal growth, similar to other capping agents used in the literature.[31,37−39] However, the detailed role of OA and OAm during crystal growth remains elusive and will be investigated in future.

The synthesis resulted in a mixture of $MAPbI_3$ nanorods (~68%), nanoplatelets (~22%), and cuboids (~10%), as is also visible in the scanning electron micrograph in Figure 1a. The bulk X-ray diffraction (XRD) pattern, shown in the upper panel of Figure 1b, matches that of the $MAPbI_3$ film prepared by conventional thermal annealing (the lower panel of Figure 1b),

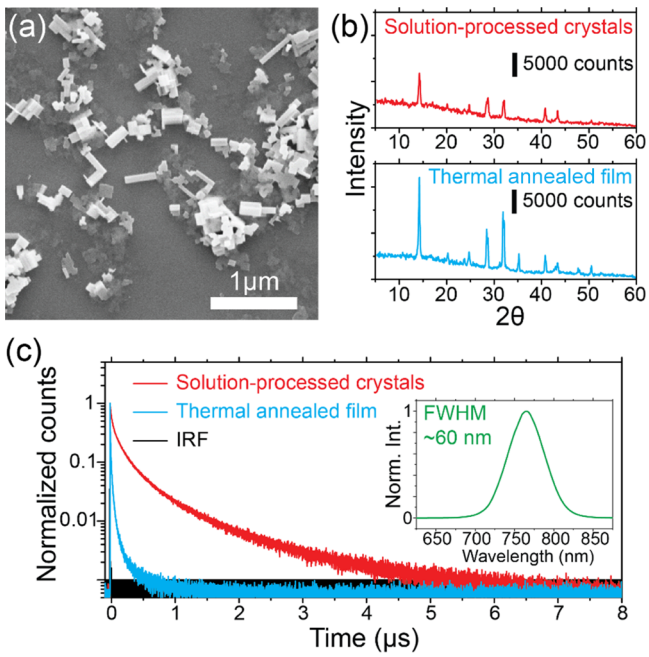

Figure 1. (a) Scanning electron micrograph of the synthesized perovskite nanocrystals. (b) XRD patterns of solution-processed perovskite nanocrystals and a thermal-annealed polycrystalline perovskite film. (c) Time-resolved PL decay histogram measured on an individual perovskite nanorod (red curve) and thermal-annealed polycrystalline perovskite films (cyan curve) under 485 nm pulsed excitation with an average power density of 80 mW/cm^2. The repetition rate was 100 kHz. The instrumental response function (IRF) is shown in black (FWHM ≈ 0.4 ns). The red decay curve can be fitted with three exponential decay components of 665.5 ns (10%), 143.4 ns (51%), and 22.2 ns (39%). The cyan decay curve can be fitted with three exponential decay components of 65.3 ns (4%), 13.5 ns (31%), and 2.2 ns (65%). The inset shows the emission spectrum of bulk perovskite nanocrystals (FWHM ≈ 60 nm).

DOI: 10.1021/acsomega.6b00107
ACS Omega 2016, 1, 148−159

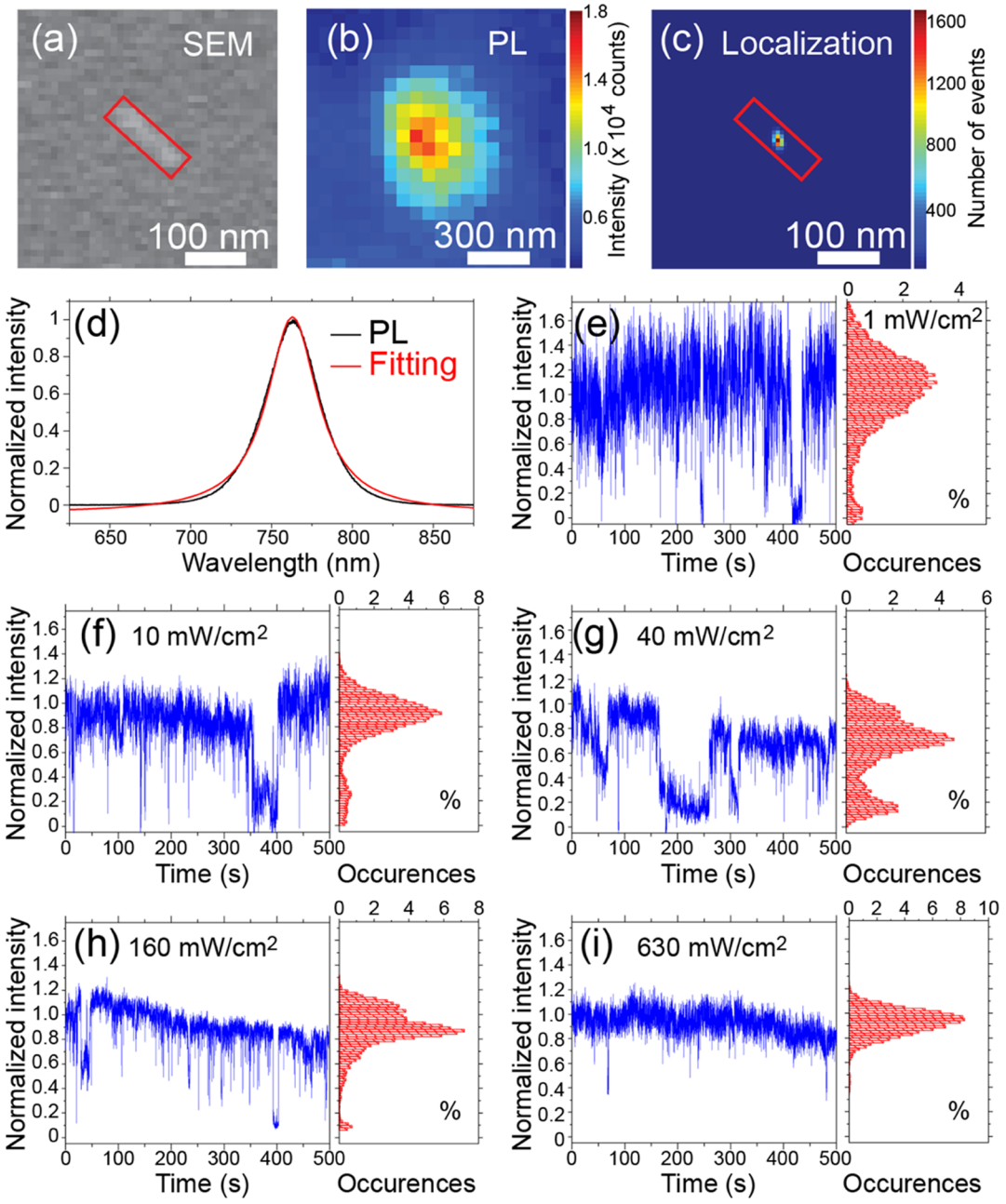

Figure 2. (a) Scanning electron micrograph of an individual perovskite nanorod, 140 nm in length and 40 nm in width. (b) PL image of the same perovskite nanorod. (c) Plot of the localization events by applying 2D Gaussian fitting. (d) PL spectrum of the same perovskite nanorod. The red curve is a Lorentzian fitting. (e–i) PL time traces (normalized intensities) and the corresponding intensity histograms (in percentage) of the same perovskite nanorod under different excitation power densities, that is, 1, 10, 40, 160, and 630 mW/cm^2.

confirming the crystalline nature of $MAPbI_3$ nanocrystals. The average dimensions of the nanorods are 160 ± 80 nm in length, 35 ± 20 nm in width, and 32 ± 12 nm in thickness [deduced from SEM and atomic force microscopy (AFM) measurements], well below the diffraction limit. Although their physical dimensions are broadly distributed, these nanocrystals show little variation in their PL emission peak wavelengths (763 ± 2 nm). However, we do notice that the individual nanorods have a narrower full-width at half-maximum (FWHM) of ∼40 nm (Figure 2d) in comparison with the PL spectrum of a bulk sample shown in Figure 1c inset (∼60 nm).

Remarkably, the individual $MAPbI_3$ nanorods showed PL lifetimes that are about 1 order of magnitude longer than those observed on the polycrystalline $MAPbI_3$ films under identical experimental conditions (a 100 kHz repetition rate and an excitation power density of 80 mW/cm^2). Figure 1c shows the PL decay histogram of an individual nanorod (the red curve) and that of a polycrystalline film prepared by the conventional thermal-annealing method (the cyan curve). Both decay curves were fitted with a triple-exponential function.[40,41] The individual nanorod reveals characteristic decay times of 665.5, 143.4, and 22.2 ns. The polycrystalline film sample that we measured for comparison showed characteristic decay times of 65.3, 13.5, and 2.2 ns. The longer PL lifetimes observed on the individual nanorods are inherently related to an improved crystallinity associated with the reduced defect density and

DOI: 10.1021/acsomega.6b00107
ACS Omega 2016, 1, 148–159

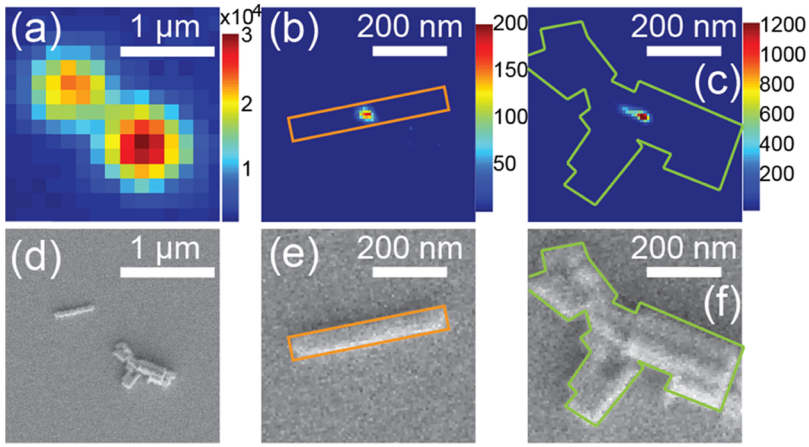

Figure 3. (a) PL image of two bright spots. The spot on the left side is because of the PL emission from an individual perovskite nanorod. The spot on the right side comes from a random cluster of several perovskite nanorods. The corresponding scanning electron micrograph on the same sample area is given in (d). The color bar shows the PL intensity in the unit of counts per frame (50 ms). The excitation power density was 16 mW/cm^2. (b and c) Plots of super-resolution localization events over the two bright spots in (a). The color bars represent the numbers of localization events. (e and f) scanning electron micrographs of the two nanostructures that correspond to (b) and (c), respectively. Solid lines in orange and in green colors outline the two nanostructures, respectively.

longer charge diffusion lengths.[10,13,30,42] Moreover, it is noteworthy that the PL lifetimes of individual nanorods differ from each other, likely due to variations in defect densities in each nanocrystal. On average, individual $MAPbI_3$ nanorods showed characteristic PL decay times of 485 ± 270, 127 ± 79, and 23 ± 13 ns.

PL of Individual $MAPbI_3$ Nanorods under Ambient Conditions. Figure 2 shows the PL of an individual nanorod under continuous-wave (CW) laser illumination. The nanorod in Figure 2a is 150 nm in length and 40 nm in width. The PL intensity image of the nanorod, given in Figure 2b, closely resembles a 2D Gaussian PSF, with a slight elongation along the longitudinal axis of the nanorod. The observed elongation is due to the fact that the nanorod (150 nm in length) is comparable in size with the diffraction-limited in our experiments (~180 nm). Therefore, the nanorod cannot be treated as an ideal point emitter. Nevertheless, 2D Gaussian is still a reasonable approximation of the PSF in this case. In particular, the localization fitting will yield widths that are sensitive to changes in the shape of the PSF and emission center positions that are sensitive to changes in quenching or emission sites. Applying a 2D Gaussian fitting on the observed emission patterns for localizing the center of mass of the emission over 10 000 frames resulted in a spread of localizations within a 10 nm radius around the geometrical center of the nanorod (Figure 2c). Even though PL blinking was observed on the nanorod (Figure 2e–i), the localization position and widths of Gaussian fittings did not show apparent changes throughout the entire measurement, regardless of the PL intensity changes during blinking (Figure S1), suggesting little changes in the nanorod PSF during PL blinking. Such observations from super-resolution localization microscopy are in contrast to the report by Tian et al.,[7] where super-resolution localization microscopy revealed changes in the positions of the localization centers alongside PL blinking in most of the studied nanostructures. The difference in observations could be related to the presence of multiple crystal grains within a diffraction-limited area in nanostructures prepared by the conventional film preparation method in the work of Tian et al.[7] This point will be further demonstrated and discussed in a later section, Super-Resolution Localization Microscopy on Individual Nanorods and Nanorod Clusters (vide infra), and is also shown in Figures S1–S3.

Next, we look into the temporal evolutions in the PL intensity of the same single-crystal nanorod. The nanorod was not exposed to laser light or electron beam irradiation before optical measurements. The nanorod PL was first measured under a low laser excitation power density of 1 mW/cm^2, which is approximately one-hundredth of the typical solar power density at the earth's surface. Because of the large absorption coefficient of $MAPbI_3$, the light penetration depth is constrained so that surface-related phenomena dominate the experimental observations at this low excitation power density. PL blinking observed at a very low light excitation power readily implies that the surface defects or traps play an important role. The laser excitation power density was then gradually increased to 10, 40, 160, and 630 mW/cm^2. At each excitation power density, the PL of the nanorod was recorded for a fixed duration of 500 s, with a frame integration time of 50 ms. The corresponding normalized PL intensity time traces are given in Figure 2e–i, respectively. PL blinking was observed on this nanorod under all excitation power densities. However, the PL intensity levels, intensity histograms, blinking frequencies, and OFF-time durations at these different illumination power densities vary largely. Under a low excitation power density of 1 mW/cm^2, the PL blinking between two steady intensity levels (ON and OFF) is clearly distinguishable in both the intensity time trace and the intensity histogram in Figure 2e. It is worth noticing that the nanorod does not become completely nonemissive in its OFF state. In many cases, the OFF-state intensity is less than one-fifth of that of the ON state (Figures 2 and S1).

Surprisingly, the often-reported "light soaking" or "photo-brightening" that describes a significant increase in PL intensity upon light illumination[7,40,43] was not observed in this experiment on individual nanorods. The "photo-brightening" phenomenon reported in the literature is often related to the high density of traps in perovskites prepared by the conventional method and their passivation by a yet-unclear photo-induced mechanism.[7,43,44] Therefore, the rare observa-

DOI: 10.1021/acsomega.6b00107
ACS Omega 2016, 1, 148–159

tion of "photo-brightening" on single-crystalline OHP nanocrystals, which was also noticed by Zhu et al.,[31] is most likely a consequence of inherently lower trap densities in the $MAPbI_3$ nanorods, which is also evident from the long PL lifetimes (Figure 1c).

Upon increasing the laser excitation power density, we noticed significant changes in the ON state of the PL intensity time traces (Figure 2f–i). Intermediate PL blinking levels that differ from the previously observed ON/OFF states started to appear in the intensity histograms (Figure 2f–h). The fluctuation in the ON-state intensity occurred in a continuous fashion, which is different than the single-step PL blinking. Moreover, it started to appear only when elevated excitation powers were applied but not at the lowest excitation power density of 1 mW/cm^2 (Figure 2e). Therefore, the changes in the ON-state intensity are likely due to the photo-induced process and of different origin than PL blinking. Photodegradation, on the other hand, is unlikely because of the low laser excitation power densities applied in these experiments; the applied power densities here are two orders of magnitude lower than those reported to cause distinct photo-degradation (tens of W/cm^2) within the measurement duration of hundreds of seconds.[15,45] Moreover, photo-induced changes in the ON-state intensity of PL blinking were mostly observed under ambient conditions, in the presence of air, but were rarely observed in vacuum. These observations indicate that the presence of oxygen and water vapor in air plays an important role, likely related to the photochemical reactions at the perovskite crystal surface.[40,46−49] A detailed discussion on this point can be found in a later section, where PL blinking under different environmental conditions is reported (Figure 6).

Super-Resolution Localization Microscopy on Individual Nanorods and Nanorod Clusters. Super-resolution localization results on individual nanorods and clusters of nanorods are compared in Figure 3. Figure 3a shows a PL image of two $MAPbI_3$ nanostructures, whose morphology can be seen in Figure 3d. The two PL emitting structures are an individual nanorod (420 nm in length and 60 nm in width) and a nanorod cluster (about 500 nm in dimension). Both nanostructures showed symmetric PSFs that are larger than the diffraction limit due to their large dimensions. Applying Gaussian approximation on their PSFs, localization results are illustrated in Figure 3b,c, respectively. The individual nanorods showed a single localization position at the center of the nanorod, even though the nanorod length clearly exceeded the diffraction limit (~180 nm). The widths of the Gaussian fitting (~250 nm) at the ON state were almost constant throughout the entire measurement (Figure S2), which indicates an almost static PSF of the ON state during the nanorod PL blinking. The PL image acquired by averaging several frames during the OFF state (Figure S1c) showed an almost identical PSF as that of the ON state. Furthermore, localization fitting on the same nanorod at different PL blinking states yielded overlaid emission center position (Figure S1). The dim PL intensities of the OFF events lead to less accurate position determination and thus broader distributions. Nevertheless, localization positions at the OFF events spread closely around the localization center position of the ON state (Figure S1f). These observations indicated that the entire rod, up to several hundred nanometers in length, blinks as one whole structure. Generally, it agrees with the earlier reports.[7,50] However, contrary to those studies, we did not observe clear shifts of the emission localization positions accompanied by PL intensity fluctuations. At the moment, we speculate that the observed differences may be related to our different sample preparation methods.

In contrast, localization on the cluster of a few nanorods revealed an elongated shape in the histogram plot (Figure 3c). Not only were multiple blinking intensity levels observed for the cluster, the Gaussian fittings also varied in width over time (Figure S2). This indicates changes in PSFs that are most likely due to stochastic blinking of each nanorod within the cluster. Therefore, the elongation in the localization found in the cluster is thus due to mixed PSFs of the closely located blinking nanorods.

Power-Law Distributions of the ON and OFF Times. Figure 4 shows statistics of the ON and OFF times of blinking events recorded on 14 individual nanorods. Time traces of each nanorod were recorded for 500 s at each excitation power density. The PL blinking OFF time and ON time histograms of the individual $MAPbI_3$ nanorods showed clear power-law distributions as illustrated in Figure 4a,b. Power-law emission intermittency, which has been generally observed on single-quantum emitters,[51−58] can be expressed by the formula $p(t_{OFF/ON}) \propto t^{\alpha}$, that is, the probability of ON or OFF times $p(t_{OFF/ON})$ is proportional to the time interval t with an exponent α. As demonstrated in Figure 4a,b, the power-law exponent (α) of both ON time and OFF time is independent of the applied laser excitation power density. The ON- and OFF-time distributions can be well simulated by the power-law exponent $\alpha = -1.6$ and -1.9, respectively. To the best of our knowledge, the power-law blinking behavior of individual $MAPbI_3$ nanorods is revealed for the first time. The revealed power-law distributions of the ON and OFF times are direct evidence for the presence of trapping and detrapping processes.[43,59]

Both the total number of OFF events and duration of OFF times were found to decrease when the laser excitation power density was increased, as can be recognized from the OFF-time histograms in Figure 4a. Although this effect as such has been reported and suggested to occur because of trap filling,[7] a quantitative assessment as presented here has been missing. Red solid lines, as guide for the eye, highlight the shift of histograms toward fewer occurrences and shorter OFF times upon higher excitation power densities. When the power density was increased from 1 to 160 mW/cm^2, the total number of OFF events reduced by a factor of 2; the average OFF time decreased from 1.16 to 0.76 s; and the longest OFF time reduced from 93.8 to 14 s. In addition, PL blinking became very rare when increasing the excitation power density above 2 W/cm^2.

Correlation between PL Decay Time and Intensity of Individual Nanorods. PL decay times were found to correlate with PL intensity during PL blinking of individual nanorods, as shown in Figure 5. Figure 5a displays an intensity time trace (red) of an individual nanorod and the corresponding average photon arrival times (blue), with a bin time of 1 s. Average photon arrival times were found to shorten when the PL intensity dropped. The ON state yielded average photon arrival times around 300 ns, whereas the OFF state yielded them around 283 ns. The scatter plot of the average photon arrival times within 1 s time bins versus the PL intensity is shown in Figure 5b. A correlation between the PL intensity and average arrival times can be clearly observed. The normalized PL decay curves of ON and OFF states are given in Figure 5c. At the low excitation power density employed here, we did not find

DOI: 10.1021/acsomega.6b00107
ACS Omega 2016, 1, 148−159

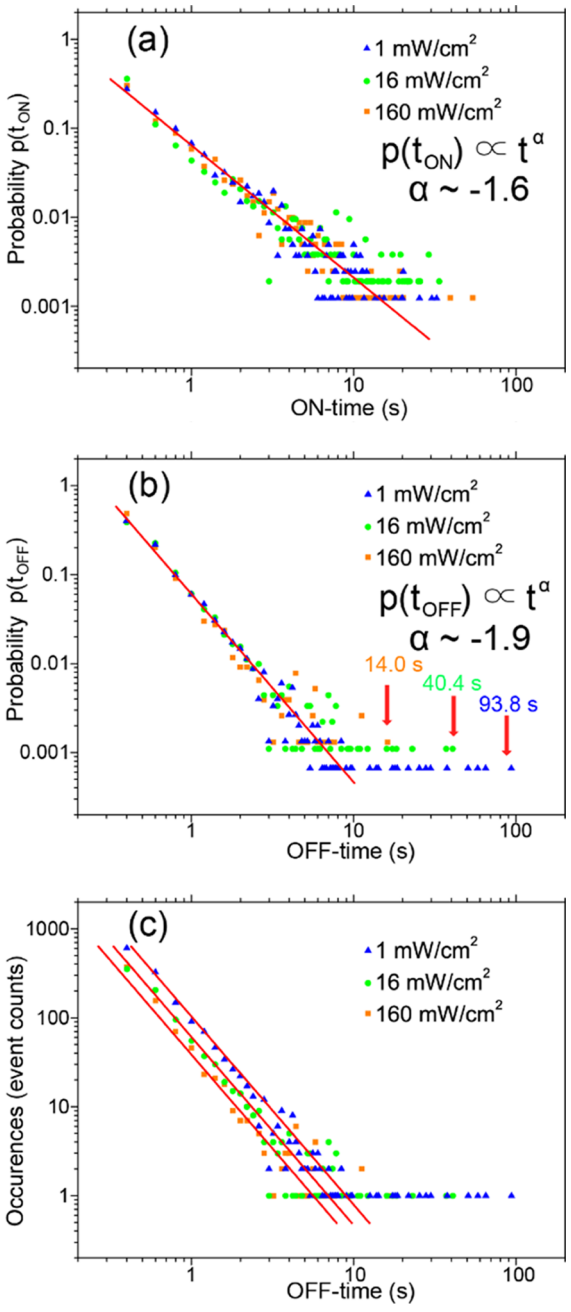

Figure 4. (a) Probability distributions of ON times under different laser excitation power densities. The red solid line shows a power-law profile with the power parameter $\alpha = -1.6$. (b) Probability distributions of OFF times under different laser excitation power densities. The red solid line shows a power-law profile with the power parameter $\alpha = -1.9$. (c) The OFF-time PL blinking histogram of 14 individual perovskite nanorods resembles the power law. Different excitation power densities were examined, that is, 1 mW/cm^2 (blue triangles), 16 mW/cm^2 (green dots), and 160 mW/cm^2 (orange squares).

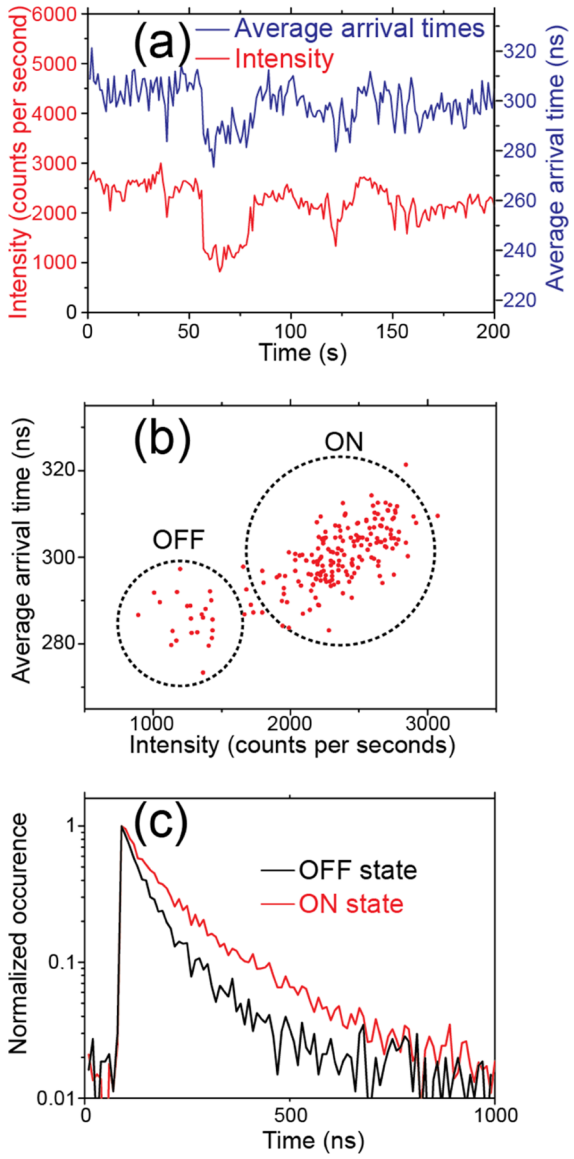

Figure 5. (a) Time traces of PL intensity (red) and average arrival times measured on an individual OHP nanorod. (b) Correlation scattered plot of average arrival times versus PL intensities. Dashed cycles are used to highlight the ON and OFF states. (c) PL decay time histograms of ON and OFF states.

changes in the PL decay times to be correlated with ON/OFF states as a function of time nor any correlation between OFF-state decay times and OFF times.

The shortened average PL decay time found at the OFF states indicates the presence of rapid nonradiative pathways. One commonly reported mechanism is Auger recombination, which is often found in the PL blinking of semiconductor quantum dots[60] and inorganic perovskite quantum dots.[58] The Auger recombination pathways in the charged states of these systems facilitate rapid nonradiative decay, resulting in prominently faster decay in the OFF state connected to PL blinking.[58,60,61] However, PL blinking here showed only minor shortening in PL decay in conjunction with the OFF state (Figure 5c), in contrast to what is expected for Auger recombination. Nevertheless, it is difficult to exclude the presence of Auger recombination. It is noteworthy that the OFF states found during PL blinking were not completely dark, which may indicate that the traps affect only a part of the nanocrystals. If this is the case, the Auger recombination can be overwhelmed by the emission that is not affected by the traps. This point requires further investigation.

On the other hand, PL blinking linked to mechanisms other than Auger recombination,[60,62,63] resulting only in minor changes in PL decay, has also been reported and attributed to "electron-accepting surface sites"[60] or charge carrier traps

DOI: 10.1021/acsomega.6b00107
ACS Omega 2016, 1, 148−159

that are associated with the surface of quantum dots where coordination of ions is incomplete.[61,62] Therefore, the observation of minor changes of PL decay alongside OHP nanorods PL blinking in this study is likely related to surface defects or surface charge trap sites, similar to their semiconductor quantum dot counterparts. If this is the case, it can be expected that the environment that surrounds the crystal can have an important impact on the PL blinking behavior.

PL of $MAPbI_3$ Nanorods in Different Atmospheres. PL blinking of nanorods is strongly dependent on the atmosphere, namely, vacuum, nitrogen, and air. Typical PL time traces of $MAPbI_3$ nanorods at different conditions are illustrated in Figure 6a–c, respectively, in vacuum (10^{-6} mbar), in nitrogen atmosphere (1 bar), and in air (1 bar, approximately 30% humidity).

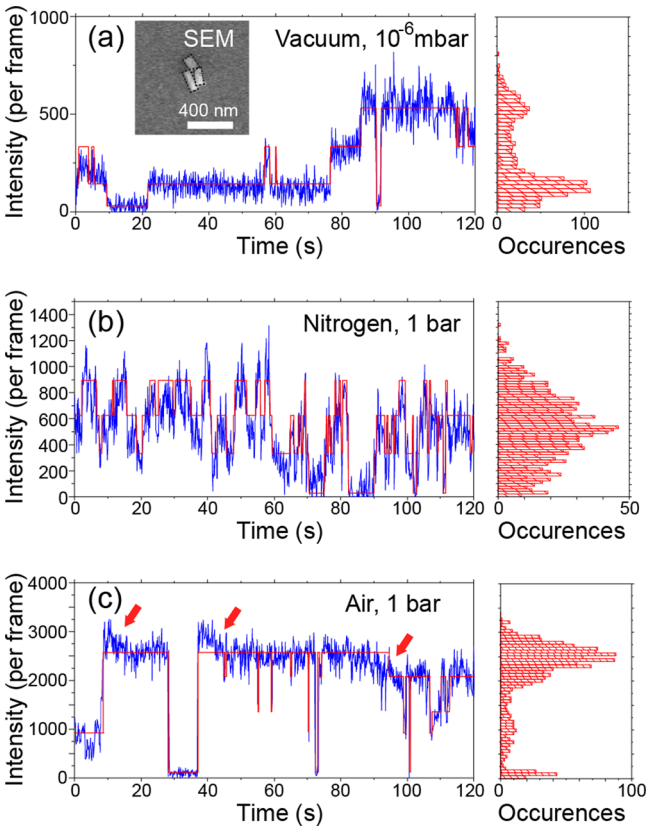

Figure 6. PL blinking time traces and histograms of perovskite nanorods under different environments, that is, under vacuum (a), in nitrogen under the ambient pressure (b), and in air under the ambient pressure (c). The same excitation power density of 16 mW/cm^2 was applied. The inset shows the scanning electron micrograph of the cluster of three perovskite nanorods. The red lines are guide for the eye, generated using vbFRET package.[64]

We next look into the effect of environment on the PL intensity of the same nanorod cluster. A cluster of three nanorods of similar dimensions can be identified in the scanning electron micrograph (inset of Figure 6a). The three nanorods are outlined with dashed lines. The PL intensity of this nanorod cluster was enhanced by more than 3 times by transferring it from vacuum (~600 counts per frame) to ambient conditions (~2800 counts per frame), as previously reported.[15] Applying state-recognizing analysis,[64] four PL intensity levels can be found in Figure 6a,b, representing the ON/OFF blinking states of the cluster in vacuum and in nitrogen. The number of levels identified corresponds well with the presence of three nanorods, each with an independent ON/OFF state. However, five intensity levels were recognized by applying the same algorithm on the same cluster in ambient atmosphere. Note that the continuous intensity fluctuations are significantly larger than the measurement noise. These intensity fluctuations in the ON-state PL are highlighted with red arrows in Figure 6c. Such fluctuations in the ON state were found on both individual nanorods (Figure 2g,h) and small clusters but only under relatively high laser excitation power densities in air. Therefore, we propose that the continuous PL intensity fluctuations of the ON state come from surface reactions involving oxygen[40,46] and/or water molecules.[48,49] Moreover, the reactions are likely enhanced by photo-generated charges and photo-induced ion mobility in the $MAPbI_3$ nanocrystals,[13] leading to an apparent excitation power dependence.

PL blinking of the same cluster behaved markedly differently in the various tested environments (vacuum, nitrogen, and air) without shifts in the emission spectrum. Blinking was found to be short-lived and most frequent in nitrogen, whereas blinking of the nanorods in air and in vacuum is less frequent. Among the three environmental conditions, vacuum resulted in the longest OFF states. In vacuum, 18 transition events between ON and OFF states among four intensity levels can be recognized within 120 s (Figure 6a). In air, the cluster showed 27 transition events in the same time window (Figure 6c). By contrast, 62 transition events were observed for the same cluster in nitrogen, which is about three times more frequent than that in vacuum or air. However, the duration of blinking OFF states in nitrogen was at most several seconds or less, which is much shorter than that observed in vacuum (tens of seconds on average) and in air (up to 10 s). The distinctly different PL blinking behaviors of the same cluster in the three different environmental conditions lead to apparent differences in the PL intensity histograms in Figure 6. The extreme sensitivity of PL blinking to the environmental conditions suggests the charge traps to be located at or close to the crystal surface. Interestingly, we also found a small fraction of nanorods whose PL blinking was less sensitive to environmental conditions. This observation implies the existence of charge traps inside of the nanocrystals as well, but with a much lower possibility. This observation supports a very recent report on trap densities on the surface of single OHP crystals that are two orders of magnitude higher than those in bulk.[65] Hence, the traps that induce PL blinking of single-crystal $MAPbI_3$ are more likely at or close to the crystal surface.

Discussion on the Possible Nature of Charge Traps. In summary, the key findings on PL blinking of perovskite nanorods are listed as follows.

(1) PL "photo-brightening" under light illumination is rarely observed on the as-synthesized $MAPbI_3$ nanorods.
(2) ON/OFF PL blinking was observed on the individual $MAPbI_3$ nanorods under low-power laser excitation.
(3) Large fluctuations in the PL ON-state intensity and multiple intensity levels appear at elevated excitation power densities under ambient conditions without leading to severe structural damage.
(4) Power-law ON-/OFF-time statistics suggest trapping and detrapping processes in PL blinking of individual nanorods.

DOI: 10.1021/acsomega.6b00107
ACS Omega 2016, 1, 148–159

(5) PL blinking of most nanorods strongly depends on their surrounding atmosphere, indicating their sensitivity to the surface charge traps. A small fraction of the nanorods show less environmental dependence on their PL blinking, suggesting the presence of trapping sites inside of the crystals.

Like other ionic materials, under-coordinated ions and vacancies may be present in single OHP crystals. On the basis of the formation mechanism, such as light-induced/charge-driven[17] or surface reactions,[66] under-coordinated ions and vacancies can be located at different positions, either inside of the crystal or on the crystal surface. Because of the low activation energies, ionic species including methylammonium ions, iodine ions, and their vacancies can be mobile in the crystal, driven by light,[17,67−69] and influence the PL properties.[13,15,16]

The surface traps that result in PL blinking of the single-crystal $MAPbI_3$ nanorods are most likely related to under-coordinated lead ions and ion vacancies. A recent study has revealed spectral shifts alongside iodine redistribution in $MAPbI_3$,[16] which indicates a high density of iodine ions in the iodine-rich regions and a high density of iodine vacancies in the iodine-poor regions. The differences in the local iodine contents are strongly correlated with the local PL emission spectra.[16] However, spectral shifts were found to be absent during $MAPbI_3$ PL blinking in this work. Moreover, photo-induced iodine migration has very recently been probed using time-of-flight secondary-ion mass spectrometry and correlated with photo-brightening without PL blinking.[13] Therefore, iodine ions/vacancies are unlikely to be responsible for PL blinking in the $MAPbI_3$ nanorods. On the other hand, Yuan et al. recently reported on instant quenching in $MAPbI_3$ PL by a focused electron beam.[15] Taking into account the organic nature of methylammonium and its low boiling point, local removal of methylammonium is a logical consequence of applying a focused electron beam on the perovskite surface, resulting in high densities of methylammonium vacancies and under-coordinated lead ions. The instant drop in PL upon applying a scanning electron beam on $MAPbI_3$ supports this assumption.[15]

Moreover, chemical surface passivation of under-coordinated lead ions has been found to enhance $MAPbI_3$ PL in several recent studies.[6,66] Therefore, besides dedicated passivation agents, surface reactions of perovskite crystals with oxygen and water have also been reported to result in passivation of under-coordinated lead ions by the formation of lead oxide and hydroxide species,[66] leading to improved PL. Such passivation by surface binding involving oxygen and water may be a contributing factor for the reported "photo-brightening" and enhancement of $MAPbI_3$ PL in air.[40,50]

The observed power-law behavior of the PL blinking ON and OFF times, in observation (4), suggests trapping and detrapping processes. In the following, we address each of our key observations one by one by proposing under-coordinated lead ions and methylammonium vacancies as possible charge traps responsible for PL blinking in $MAPbI_3$ nanorods. In this study, the excess amounts of methylammonium iodide during the synthesis and the good crystallinity of the resulting nanorods are believed to reduce the amount of under-coordinated lead ions. Under a very low laser excitation, PL blinking reflects the charge traps formed during crystal growth. Because under-coordinated lead ions are expected to be rare in the synthesized crystals in this study, the often-reported phenomenon of "photo-brightening" by passivation of under-coordinated lead ions with oxygen or water will be eliminated, as noticed in observation (1). However, PL blinking can still be observed even at a low density of under-coordinated lead ions. Because of the exceptional charge diffusion lengths up to several microns in OHP crystals,[10,42] a single charge trap may control the PL blinking of a nanosized crystal.[7,43] Therefore, PL blinking can take place even at very low charge trap densities in single-crystalline OHP nanorods, leading to observation (2).

The strong environmental dependence of PL blinking outlined in observations (3) and (5) can be related to the differences in charge trap formation probabilities because the detrapping rates in different atmospheres are different. Furthermore, charge trap formation rates are different for nanorods in different environmental conditions. Because of the low boiling points of methylammonium, detachment can be promoted by a vacuum.[70] Moreover, water vapor in air promotes the removal of methylammonium from a perovskite surface.[49,71] Therefore, both environmental conditions of vacuum and air can easily result in methylammonium vacancies and under-coordinated lead ions on the crystal surface, leading to higher charge trap formation probabilities than in an inert atmosphere. In contrast, charge trap formation in an inert nitrogen atmosphere relies only on the thermal detachment of methylammonium from the surface. Hence, the trap formation probability in nitrogen is expected to be the lowest among the three environmental conditions. On the other hand, detrapping rates can differ in different atmospheres. In vacuum and in nitrogen, detrapping most likely involves mobile ions in the crystal driven by light. In air, extra detrapping pathways by surface reactions with oxygen or water may be present. PL blinking of a nanorod is therefore controlled by trap-formation rates and detrapping rates.

It is noteworthy that the OFF state of PL blinking may not necessarily correspond to a single trap because of the ability of a single charge trap to quench the PL of an entire nanocrystal. Therefore, multiple traps could result in a long-lived OFF state, and this cannot be identified based on the intensity in this experiment. Assuming the same detrapping rates for $MAPbI_3$ nanorods in vacuum and in nitrogen, the very long OFF times observed in vacuum can be understood through the higher possibility to form multiple traps. By contrast, short-lived OFF events found on $MAPbI_3$ nanorods in nitrogen, where the trap formation rate is the lowest, are likely due to single traps, resulting in similar detrapping time (OFF time). PL blinking of nanorods in air is, however, more complex as a result of the interplay between detrapping processes by mobile ions and surface reactions, leading to broadly distributed OFF times ranging from tens of seconds to hundreds of milliseconds. However, to verify this point, further investigation is necessary.

The fluctuations in the ON-state intensity levels in air under relatively high excitation power densities found in observation (3) are most likely due to surface photochemical reactions of $MAPbI_3$ with oxygen and water. Because it occurs only at relatively high laser excitation power, such surface chemical reactions are likely promoted by light or light-generated charges.[72] This could also contribute to the absence of PL blinking at the high laser excitation power density above 2 W/cm^2. The promoted surface chemical reactions by strong laser excitation result in rapid passivation of vacancies and under-coordinated lead ions, resulting in blocking possible trapping sites.

DOI: 10.1021/acsomega.6b00107
ACS Omega 2016, 1, 148−159

In summary, the experimental observations presented in this work yielded strong evidence for the following: (i) charge traps that cause PL blinking of $MAPbI_3$ nanorods, likely methylammonium vacancies and under-coordinated lead ions; (ii) the environmental conditions surrounding the $MAPbI_3$ nanorods affect the PL blinking behavior of OHP nanorods by influencing trap formation rates and detrapping rates on the crystal surface; (iii) a single charge trap on the surface of an $MAPbI_3$ nanorod can dictate the PL blinking of the entire crystal; (iv) the OFF state during PL blinking may result from one or multiple charge traps; (iv) the light-promoted surface chemical reactions of $MAPbI_3$ with oxygen and water may lead to large variations in the ON-state PL intensity and may be responsible for the lack of PL blinking at high excitation power densities.

CONCLUSIONS

In conclusion, we demonstrated a novel approach for the synthesis of highly crystalline $MAPbI_3$ nanorods and performed a systematic investigation on the PL blinking of individual $MAPbI_3$ nanorods. We revealed two-level PL blinking of individual nanorods under low laser excitation power densities. Moreover, super-resolution localization study on these blinking nanorods shows single perovskite nanorods (several hundred nanometers) to blink and to emit as a whole, demonstrating the ability of charge traps to dominate PL emission in a single nanorod of several hundred nanometers in length, which is qualitatively in agreement with the earlier observations.[7] Furthermore, PL blinking of nanorods showed strong light illumination power dependence as well as environmental dependence that are related to charge trapping and detrapping processes, evident from the power-law behavior of the experimentally recorded ON/OFF times shown here for the first time. PL lifetime measurements suggest processes other than Auger recombination to contribute to the blinking of nanorods. On the basis of the PL blinking observations on $MAPbI_3$ nanorods in these experiments, the charge traps that are likely related to the under-coordinated lead ions and methylammonium vacancies on the crystal surface are proposed to cause the PL blinking observed here. Nevertheless, a deeper understanding on the nature of traps and the detrapping process requires further experimental and theoretical investigations.

EXPERIMENTAL SECTION

Materials. All the chemicals were used as received from Sigma-Aldrich, including lead(II) iodide (99%), hydriodic acid (57 wt % in water), methylamine (33 wt % in absolute ethanol), OA, OAm (70%, technical grade), acetonitrile, γ-butyrolactone, diethyl ether, ethanol for spectroscopy, absolute ethanol, and toluene.

Preparation of Methylammonium Iodide (CH_3NH_3I). Methylammonium iodide was synthesized by a typical procedure.[7] Methylamine (27.8 mL) and hydriodic acid (30 mL) were reacted in a 150 mL round-bottom flask at 0 °C for 2 h under stirring. The precipitate was recovered by using a rotary evaporator by removing the solvents at 50 °C. The obtained product was redissolved in 80 mL of ethanol, recrystallized by the addition of 300 mL of diethyl ether twice, and finally dissolved with absolute ethanol. Methylammonium iodide was then collected by drying at 60 °C in a vacuum oven for 24 h.

Polycrystalline Perovskite Crystals. Methylammonium iodide (92 mg) and 32 mg lead(II) iodide were dissolved in 2 mL of γ-butyrolactone at 60 °C. A perovskite film sample was prepared by spin-coating the 60 °C solution onto a glass cover slide, with a speed of 1500 rpm for 60 s. Right after spin-coating, the sample was heated at 70 °C for 10 min. The sample was then subjected to optical experiments right after preparation.

Synthesis of Perovskite Nanorods. Solution A: 2.8 μL of OAm and 5.2 μL of OA were dissolved in 5 mL of toluene. Solution B: 9.2 mg lead iodide and 9.2 mg methylammonium iodide were dissolved in 10 mL acetonitrile. Magnetic stirring (600 rpm) was applied throughout the entire synthesis. Solution B (1.3 mL) was injected into Solution A. The solution turned red in color, indicating the formation of OHP crystals of very small sizes. After 30 s, 7 mL of toluene was added to the mixed solution dropwise, after which the solution was kept under stirring in the dark for 4 h. The dark brownish suspension was then washed and redispersed in 4 mL toluene two times by centrifuging at 3000 rpm for 30 min. The final suspension was maintained in the dark.

XRD. XRD measurements on the prepared perovskite materials were carried out on a STOE STADI P COMBI instrument equipped with an imaging plate (IP position sensitive detector) as the detector. The diffraction was measured using Cu $K\alpha_1$ radiation in transmission mode with a focusing Ge(111) monochromator.

AFM. A Smart-1000 AFM (AIST-NT) was used for AFM measurements under ambient conditions in tapping mode with a Si tip (cantilever length, 140 μm; resonant frequency, 200−400 kHz; spring constant, 25−95 N/m) at a scanning rate of 0.5 Hz and a sample line of 1024.

Integrated Optical and Electron Microscope (iLEM). The iLEM system consists of an FEI Quanta FEG-250 environmental scanning electron microscope, equipped with a modified door assembly provided by Delmic BV, the Netherlands. This door features an optically transparent window which enables the transmission of excitation and emission light and holds both an EM-CCD camera (Image-EM X2, Hamamatsu) and optomechanics. Additionally, the original SEM stage is replaced by one that is capable of holding a high-numerical-aperture oil-immersion objective lens (Plan Apo VC 100×, NA 1.4, Nikon), which enables high-resolution imaging in combination with vacuum-compatible immersion oil. The ILEM instrument is further equipped with a laser illumination system featuring six distinct continuous-wave laser sources (405, 445, 488, 532, 561, and 642 nm, LightHub, Omicron). The 532 nm output is employed as the excitation source in this study. A compact spectrometer (USB4000, Ocean Optics) is used for spectral measurements. Super-resolution localization fitting was applied using a set of home-developed Matlab code. A detailed description can be found in previous reports.[73,74] PL time traces shown in Figure 2 were normalized by the initial ON-state intensity after background subtraction. Half the ON-state intensity was used as the threshold to determine the ON/OFF times.

Confocal Optical Microscope for Time-Resolved Measurements. The confocal microscopy results were obtained on an inverted optical microscope (Olympus IX71) equipped with a set of galvo scanning mirrors (Yanus IV, Till Photonics, Chromaphor). A pulsed 485 nm laser (PicoQuant, LDH-D-C-485) was used as the excitation source. Laser repetition rates of 100 kHz or 1 MHz were applied. Circular

DOI: 10.1021/acsomega.6b00107
ACS Omega 2016, 1, 148−159

polarization at the sample was achieved by a set of half-wavelength ($\lambda/2$) and quarter-wavelength ($\lambda/4$) waveplates. An oil-immersion objective lens from Olympus which has a numerical aperture of 1.4 and 100× magnification was used. Time-resolved single-photon counting (TCSPC) data were acquired with fiber-coupled avalanche photon diodes and a HydraHarp 400 system (PicoQuant).

Sample Preparation. For SEM characterization, 5 μL of OHP nanorod suspension was drop-casted onto a 5 mm × 5 mm silicon chip and was dried in a fume hood. For AFM measurements, 100 μL was dropped onto a clean glass cover slide for about 60 s and was then dried by a nitrogen flow. For optical measurements, 100 μL of OHP nanorod toluene suspension was dropped onto a clean glass cover slide and was spin-casted at 1500 rpm for 60 s. For correlative SEM measurements after optical experiments, the sample was coated with a thin gold film using a JOEL auto fine film coater.

■ ASSOCIATED CONTENT

Supporting Information

The Supporting Information is available free of charge on the ACS Publications website at DOI: 10.1021/acsomega.6b00107.

PL intensity correlated super-resolution localization mapping on a single-crystal $MAPbI_3$ nanorod, Gaussian fitting widths time evolution during PL blinking of a single-crystal nanorod and a cluster of several nanorods, super-resolution localization mapping on polycrystalline deposits, and PL decays of nanorods and polycrystalline films (PDF)

■ AUTHOR INFORMATION

Corresponding Authors

*E-mail: haifeng.yuan@chem.kuleuven.be (H.Y.).

*E-mail: maarten.roeffaers@biw.kuleuven.be (M.B.J.R.).

Notes

The authors declare no competing financial interest.

■ ACKNOWLEDGMENTS

We thank Prof. Ivan Scheblykin and his co-workers as well as Dr. Rafael Camacho for stimulating discussions. We thank Marike Wolberg for assistance with the XRD measurements. We acknowledge financial support from the Research Foundation-Flanders (FWO, grant G.0197.11, G.0962.13, G0B39.15, postdoctoral fellowship to H.Y., E.D., and K.P.F.J.), KU Leuven Research Fund (OT/12/059 and C14/15/053), the Flemish government through long-term structural funding Methusalem (CASAS^2, Meth/15/04), the Hercules foundation (HER/11/14), the Belgian Federal Science Policy Office (IAP-PH05), the EC through the Marie Curie ITN project iSwitch (GA-642196), and the ERC projects LIGHT (GA-307523).

■ REFERENCES

(1) Yang, W. S.; Noh, J. H.; Jeon, N. J.; Kim, Y. C.; Ryu, S.; Seo, J.; Seok, S. I. High-performance photovoltaic perovskite layers fabricated through intramolecular exchange. *Science* **2015**, *348*, 1234−1237.

(2) Saliba, M.; Orlandi, S.; Matsui, T.; Aghazada, S.; Cavazzini, M.; Correa-Baena, J.-P.; Gao, P.; Scopelliti, R.; Mosconi, E.; Dahmen, K.-H.; De Angelis, F.; Abate, A.; Hagfeldt, A.; Pozzi, G.; Graetzel, M.; Nazeeruddin, M. K. A molecularly engineered hole-transporting material for efficient perovskite solar cells. *Nat. Energy* **2016**, *1*, 15017.

(3) Park, N. G. Perovskite solar cells: an emerging photovoltaic technology. *Mater. Today* **2015**, *18*, 65−72.

(4) Yusoff, A. R. b. M.; Nazeeruddin, M. K. Organohalide lead perovskites for photovoltaic applications. *J. Phys. Chem. Lett.* **2016**, *7*, 851−866.

(5) Sharenko, A.; Toney, M. F. Relationships between lead halide perovskite thin-film fabrication, morphology, and performance in solar cells. *J. Am. Chem. Soc.* **2016**, *138*, 463−470.

(6) deQuilettes, D. W.; Vorpahl, S. M.; Stranks, S. D.; Nagaoka, H.; Eperon, G. E.; Ziffer, M. E.; Snaith, H. J.; Ginger, D. S. Impact of microstructure on local carrier lifetime in perovskite solar cells. *Science* **2015**, *348*, 683−686.

(7) Tian, Y.; Merdasa, A.; Peter, M.; Abdellah, M.; Zheng, K.; Ponseca, C. S.; Pullerits, T.; Yartsev, A.; Sundström, V.; Scheblykin, I. G. Giant photoluminescence blinking of perovskite nanocrystals reveals single-trap control of luminescence. *Nano Lett.* **2015**, *15*, 1603−1608.

(8) Li, Y.; Yan, W.; Li, Y.; Wang, S.; Wang, W.; Bian, Z.; Xiao, L.; Gong, Q. Direct observation of long electron-hole diffusion distance in $CH_3NH_3PbI_3$ perovskite thin film. *Sci. Rep.* **2015**, *5*, 14485.

(9) Tian, W.; Zhao, C.; Leng, J.; Cui, R.; Jin, S. Visualizing carrier diffusion in individual single-crystal organolead halide perovskite nanowires and nanoplates. *J. Am. Chem. Soc.* **2015**, *137*, 12458−12461.

(10) Stranks, S. D.; Eperon, G. E.; Grancini, G.; Menelaou, C.; Alcocer, M. J. P.; Leijtens, T.; Herz, L. M.; Petrozza, A.; Snaith, H. J. Electron-hole diffusion lengths exceeding 1 micrometer in an organometal trihalide perovskite absorber. *Science* **2013**, *342*, 341−344.

(11) Christians, J. A.; Manser, J. S.; Kamat, P. V. Multifaceted excited state of $CH_3NH_3PbI_3$. Charge separation, recombination, and trapping. *J. Phys. Chem. Lett.* **2015**, *6*, 2086−2095.

(12) Stranks, S. D.; Burlakov, V. M.; Leijtens, T.; Ball, J. M.; Goriely, A.; Snaith, H. J. Recombination kinetics in organic−inorganic perovskites: excitons, free charge, and subgap states. *Phys. Rev. Appl.* **2014**, *2*, 034007.

(13) deQuilettes, D. W.; Zhang, W.; Burlakov, V. M.; Graham, D. J.; Leijtens, T.; Osherov, A.; Bulović, V.; Snaith, H. J.; Ginger, D. S.; Stranks, S. D. Photo-induced halide redistribution in organic−inorganic perovskite films. *Nat. Commun.* **2016**, *7*, 11683.

(14) Bischak, C. G.; Sanehira, E. M.; Precht, J. T.; Luther, J. M.; Ginsberg, N. S. Heterogeneous charge carrier dynamics in organic−inorganic hybrid materials: nanoscale lateral and depth-dependent variation of recombination rates in methylammonium lead halide perovskite thin films. *Nano Lett.* **2015**, *15*, 4799−4807.

(15) Yuan, H.; Debroye, E.; Janssen, K.; Naiki, H.; Steuwe, C.; Lu, G.; Moris, M.; Orgiu, E.; Uji-i, H.; De Schryver, F.; Samorì, P.; Hofkens, J.; Roeffaers, M. Degradation of methylammonium lead iodide perovskite structures through light and electron beam driven ion migration. *J. Phys. Chem. Lett.* **2016**, *7*, 561−566.

(16) Hentz, O.; Zhao, Z.; Gradečak, S. Impacts of ion segregation on local optical properties in mixed halide perovskite films. *Nano Lett.* **2016**, *16*, 1485−1490.

(17) Meloni, S.; Moehl, T.; Tress, W.; Franckevičius, M.; Saliba, M.; Lee, Y. H.; Gao, P.; Nazeeruddin, M. K.; Zakeeruddin, S. M.; Rothlisberger, U.; Graetzel, M. Ionic polarization-induced current−voltage hysteresis in $CH_3NH_3PbX_3$ perovskite solar cells. *Nat. Commun.* **2016**, *7*, 10334.

(18) Xiao, Z.; Yuan, Y.; Shao, Y.; Wang, Q.; Dong, Q.; Bi, C.; Sharma, P.; Gruverman, A.; Huang, J. Giant switchable photovoltaic effect in organometal trihalide perovskite devices. *Nat. Mater.* **2014**, *14*, 193−198.

(19) Draguta, S.; Thakur, S.; Morozov, Y. V.; Wang, Y.; Manser, J. S.; Kamat, P. V.; Kuno, M. Spatially non-uniform trap state densities in solution-processed hybrid perovskite thin films. *J. Phys. Chem. Lett.* **2016**, *7*, 715−721.

(20) Klein, J. R.; Flender, O.; Scholz, M.; Oum, K.; Lenzer, T. Charge carrier dynamics of methylammonium lead iodide: from PbI_2-rich to low-dimensional broadly emitting perovskites. *Phys. Chem. Chem. Phys.* **2016**, *18*, 10800−10808.

(21) Liu, M.; Johnston, M. B.; Snaith, H. J. Efficient planar heterojunction perovskite solar cells by vapour deposition. *Nature* **2013**, *501*, 395−398.
(22) Kutes, Y.; Zhou, Y.; Bosse, J. L.; Steffes, J.; Padture, N. P.; Huey, B. D. Mapping the photoresponse of $CH_3NH_3PbI_3$ hybrid perovskite thin films at the nanoscale. *Nano Lett.* **2016**, *16*, 3434−3441.
(23) Li, C.; Tscheuschner, S.; Paulus, F.; Hopkinson, P. E.; Kießling, J.; Köhler, A.; Vaynzof, Y.; Huettner, S. Iodine migration and its effect on hysteresis in perovskite solar cells. *Adv. Mater.* **2016**, *28*, 2446−2454.
(24) Yun, J. S.; Ho-Baillie, A.; Huang, S.; Woo, S. H.; Heo, Y.; Seidel, J.; Huang, F.; Cheng, Y.-B.; Green, M. A. Benefit of grain boundaries in organic−inorganic halide planar perovskite solar cells. *J. Phys. Chem. Lett.* **2015**, *6*, 875−880.
(25) Shao, Y.; Fang, Y.; Li, T.; Wang, Q.; Dong, Q.; Deng, Y.; Yuan, Y.; Wei, H.; Wang, M.; Gruverman, A.; Shield, J.; Huang, J. Grain boundary dominated ion migration in polycrystalline organic−inorganic halide perovskite films. *Energy Environ. Sci.* **2016**, *9*, 1752−1759.
(26) González-Carrero, S.; Galian, R. E.; Pérez-Prieto, J. Organometal halide perovskites: bulk low-dimension materials and nanoparticles. *Part. Part. Syst. Charact.* **2015**, *32*, 709−720.
(27) González-Carrero, S.; Galian, R. E.; Pérez-Prieto, J. Organic−inorganic and all-inorganic lead halide nanoparticles. *Opt. Express* **2016**, *24*, A285−A301.
(28) Schmidt, L. C.; Pertegás, A.; González-Carrero, S.; Malinkiewicz, O.; Agouram, S.; Espallargas, G. M.; Bolink, H. J.; Galian, R. E.; Pérez-Prieto, J. Nontemplate synthesis of $CH_3NH_3PbBr_3$ perovskite nanoparticles. *J. Am. Chem. Soc.* **2014**, *136*, 850−853.
(29) Zhu, H.; Fu, Y.; Meng, F.; Wu, X.; Gong, Z.; Ding, Q.; Gustafsson, M. V.; Trinh, M. T.; Jin, S.; Zhu, X.-Y. Lead halide perovskite nanowire lasers with low lasing thresholds and high quality factors. *Nat. Mater.* **2015**, *14*, 636−642.
(30) Fu, Y.; Meng, F.; Rowley, M. B.; Thompson, B. J.; Shearer, M. J.; Ma, D.; Hamers, R. J.; Wright, J. C.; Jin, S. Solution growth of single crystal methylammonium lead halide perovskite nanostructures for optoelectronic and photovoltaic applications. *J. Am. Chem. Soc.* **2015**, *137*, 5810−5818.
(31) Zhu, F.; Men, L.; Guo, Y.; Zhu, Q.; Bhattacharjee, U.; Goodwin, P. M.; Petrich, J. W.; Smith, E. A.; Vela, J. Shape evolution and single particle luminescence of organometal halide perovskite nanocrystals. *ACS Nano* **2015**, *9*, 2948−2959.
(32) Aharon, S.; Etgar, L. Two dimensional organometal halide perovskite nanorods with tunable optical properties. *Nano Lett.* **2016**, *16*, 3230−3235.
(33) González-Carrero, S.; Galian, R. E.; Pérez-Prieto, J. Maximizing the emissive properties of $CH_3NH_3PbBr_3$ perovskite nanoparticles. *J. Mater. Chem. A* **2015**, *3*, 9187−9193.
(34) Huang, B.; Bates, M.; Zhuang, X. Super-resolution fluorescence microscopy. *Annu. Rev. Biochem.* **2009**, *78*, 993−1016.
(35) Habuchi, S. Super-resolution molecular and functional imaging of nanoscale architectures in life and materials science. *Front. Bioeng. Biotechnol.* **2014**, *2*, 20.
(36) Neely, R. K.; Dedecker, P.; Hotta, J.-i.; Urbanavičiūtė, G.; Klimašauskas, S.; Hofkens, J. DNA fluorocode: a single molecule, optical map of DNA with nanometre resolution. *Chem. Sci.* **2010**, *1*, 453−460.
(37) Chen, Y.; He, M.; Peng, J.; Sun, Y.; Liang, Z. Structure and growth control of organic−inorganic halide perovskites for optoelectronics: From polycrystalline films to single crystals. *Adv. Sci.* **2016**, *3*, 1500392.
(38) De Roo, J.; Ibáñez, M.; Geiregat, P.; Nedelcu, G.; Walravens, W.; Maes, J.; Martins, J. C.; Van Driessche, I.; Kovalenko, M. V.; Hens, Z. Highly dynamic ligand binding and light absorption coefficient of cesium lead bromide perovskite nanocrystals. *ACS Nano* **2016**, *10*, 2071−2081.
(39) Ma, Q.; Mimura, K. i.; Kato, K. Tuning shape of barium titanate nanocubes by combination of oleic acid/tert-butylamine through hydrothermal process. *J. Alloys Compd.* **2016**, *655*, 71−78.
(40) Tian, Y.; Peter, M.; Unger, E.; Abdellah, M.; Zheng, K.; Pullerits, T.; Yartsev, A.; Sundström, V.; Scheblykin, I. G. Mechanistic insights into perovskite photoluminescence enhancement: light curing with oxygen can boost yield thousandfold. *Phys. Chem. Chem. Phys.* **2015**, *17*, 24978−24987.
(41) Kim, B. J.; Kim, D. H.; Lee, Y.-Y.; Shin, H.-W.; Han, G. S.; Hong, J. S.; Mahmood, K.; Ahn, T. K.; Joo, Y.-C.; Hong, K. S.; Park, N.-G.; Lee, S.; Jung, H. S. Highly efficient and bending durable perovskite solar cells: toward a wearable power source. *Energy Environ. Sci.* **2015**, *8*, 916−921.
(42) Shi, D.; Adinolfi, V.; Comin, R.; Yuan, M.; Alarousu, E.; Buin, A.; Chen, Y.; Hoogland, S.; Rothenberger, A.; Katsiev, K.; Losovyj, Y.; Zhang, X.; Dowben, P. A.; Mohammed, O. F.; Sargent, E. H.; Bakr, O. M. Low trap-state density and long carrier diffusion in organolead trihalide perovskite single crystals. *Science* **2015**, *347*, 519−522.
(43) Ponseca, C. S., Jr.; Tian, Y.; Sundström, V.; Scheblykin, I. G. Excited state and charge-carrier dynamics in perovskite solar cell materials. *Nanotechnology* **2016**, *27*, 082001.
(44) Wen, X.; Feng, Y.; Huang, S.; Huang, F.; Cheng, Y.-B.; Green, M.; Ho-Baillie, A. Defect trapping states and charge carrier recombination in organic−inorganic halide perovskites. *J. Mater. Chem. C* **2016**, *4*, 793−800.
(45) Merdasa, A.; Bag, M.; Tian, Y.; Källman, E.; Dobrovolsky, A.; Scheblykin, I. G. Super-resolution luminescence micro-spectroscopy reveals mechanism of photoinduced degradation in $CH_3NH_3PbI_3$ perovskite nanocrystals. *J. Phys. Chem. C* **2016**, *120*, 10711−10719.
(46) Kong, W.; Rahimi-Iman, A.; Bi, G.; Dai, X.; Wu, H. Oxygen intercalation induced by photocatalysis on the surface of hybrid lead halide perovskites. *J. Phys. Chem. C* **2016**, *120*, 7606−7611.
(47) Aristidou, N.; Sanchez-Molina, I.; Chotchuangchutchaval, T.; Brown, M.; Martinez, L.; Rath, T.; Haque, S. A. The role of oxygen in the degradation of methylammonium lead trihalide perovskite photoactive layers. *Angew. Chem., Int. Ed.* **2015**, *54*, 8208−8212.
(48) Müller, C.; Glaser, T.; Plogmeyer, M.; Sendner, M.; Döring, S.; Bakulin, A. A.; Brzuska, C.; Scheer, R.; Pshenichnikov, M. S.; Kowalsky, W.; Pucci, A.; Lovrinčić, R. Water infiltration in methylammonium lead iodide perovskite: fast and inconspicuous. *Chem. Mat.* **2015**, *27*, 7835−7841.
(49) Mosconi, E.; Azpiroz, J. M.; De Angelis, F. Ab initio molecular dynamics simulations of methylammonium lead iodide perovskite degradation by water. *Chem. Mat.* **2015**, *27*, 4885−4892.
(50) Tian, Y.; Merdasa, A.; Unger, E.; Abdellah, M.; Zheng, K.; McKibbin, S.; Mikkelsen, A.; Pullerits, T.; Yartsev, A.; Sundström, V.; Scheblykin, I. G. Enhanced organo-metal halide perovskite photoluminescence from nanosized defect-free crystallites and emitting sites. *J. Phys. Chem. Lett.* **2015**, *6*, 4171−4177.
(51) Cichos, F.; von Borczyskowski, C.; Orrit, M. Power-law intermittency of single emitters. *Curr. Opin. Colloid Interface Sci.* **2007**, *12*, 272−284.
(52) Frantsuzov, P.; Kuno, M.; Janko, B.; Marcus, R. A. Universal emission intermittency in quantum dots, nanorods and nanowires. *Nat. Phys.* **2008**, *4*, 519−522.
(53) Clifford, J. N.; Bell, T. D. M.; Tinnefeld, P.; Heilemann, M.; Melnikov, S. M.; Hotta, J.-i.; Sliwa, M.; Dedecker, P.; Sauer, M.; Hofkens, J.; Yeow, E. K. L. Fluorescence of single molecules in polymer films: sensitivity of blinking to local environment. *J. Phys. Chem. B* **2007**, *111*, 6987−6991.
(54) Hoogenboom, J. P.; Hernando, J.; van Dijk, E. M. H. P.; van Hulst, N. F.; García-Parajó, M. F. Power-law blinking in the fluorescence of single organic molecules. *ChemPhysChem* **2007**, *8*, 823−833.
(55) Kuno, M.; Fromm, D. P.; Hamann, H. F.; Gallagher, A.; Nesbitt, D. J. Nonexponential "blinking" kinetics of single CdSe quantum dots: a universal power law behavior. *J. Chem. Phys.* **2000**, *112*, 3117−3120.
(56) Peterson, J. J.; Nesbitt, D. J. Modified power law behavior in quantum dot blinking: a novel role for biexcitons and Auger ionization. *Nano Lett.* **2009**, *9*, 338−345.
(57) Hu, F.; Zhang, H.; Sun, C.; Yin, C.; Lv, B.; Zhang, C.; Yu, W. W.; Wang, X.; Zhang, Y.; Xiao, M. Superior optical properties of

DOI: 10.1021/acsomega.6b00107
ACS Omega 2016, 1, 148−159

perovskite nanocrystals as single photon emitters. *ACS Nano* **2015**, *9*, 12410−12416.
(58) Park, Y.-S.; Guo, S.; Makarov, N. S.; Klimov, V. I. Room temperature single-photon emission from individual perovskite quantum dots. *ACS Nano* **2015**, *9*, 10386−10393.
(59) Verberk, R.; van Oijen, A. M.; Orrit, M. Simple model for the power-law blinking of single semiconductor nanocrystals. *Phys. Rev. B* **2002**, *66*, 233202.
(60) Galland, C.; Ghosh, Y.; Steinbruck, A.; Sykora, M.; Hollingsworth, J. A.; Klimov, V. I.; Htoon, H. Two types of luminescence blinking revealed by spectroelectrochemistry of single quantum dots. *Nature* **2011**, *479*, 203−207.
(61) Rabouw, F. T.; Kamp, M.; van Dijk-Moes, R. J. A.; Gamelin, D. R.; Koenderink, A. F.; Meijerink, A.; Vanmaekelbergh, D. Delayed exciton emission and its relation to blinking in CdSe quantum dots. *Nano Lett.* **2015**, *15*, 7718−7725.
(62) Rosen, S.; Schwartz, O.; Oron, D. Transient fluorescence of the off state in blinking CdSe/CdS/ZnS semiconductor nanocrystals is not governed by Auger recombination. *Phys. Rev. Lett.* **2010**, *104*, 157404.
(63) Cordones, A. A.; Bixby, T. J.; Leone, S. R. Direct measurement of off-state trapping rate fluctuations in single quantum dot fluorescence. *Nano Lett.* **2011**, *11*, 3366−3369.
(64) Bronson, J. E.; Fei, J.; Hofman, J. M.; Gonzalez, R. L., Jr.; Wiggins, C. H. Learning rates and states from biophysical time series: a Bayesian approach to model selection and single-molecule FRET data. *Biophys. J.* **2009**, *97*, 3196−3205.
(65) Wu, B.; Nguyen, H. T.; Ku, Z.; Han, G.; Giovanni, D.; Mathews, N.; Fan, H. J.; Sum, T. C. Discerning the surface and bulk recombination kinetics of organic−inorganic halide perovskite single crystals. *Adv. Energy Mater.* **2016**, *6*, 1600551.
(66) Noel, N. K.; Abate, A.; Stranks, S. D.; Parrott, E. S.; Burlakov, V. M.; Goriely, A.; Snaith, H. J. Enhanced photoluminescence and solar cell performance via Lewis base passivation of organic−inorganic lead halide perovskites. *ACS Nano* **2014**, *8*, 9815−9821.
(67) Eames, C.; Frost, J. M.; Barnes, P. R. F.; O'Regan, B. C.; Walsh, A.; Islam, M. S. Ionic transport in hybrid lead iodide perovskite solar cells. *Nat. Commun.* **2015**, *6*, 7497.
(68) Azpiroz, J. M.; Mosconi, E.; Bisquert, J.; De Angelis, F. Defect migration in methylammonium lead iodide and its role in perovskite solar cell operation. *Energy Environ. Sci.* **2015**, *8*, 2118−2127.
(69) Klein-Kedem, N.; Cahen, D.; Hodes, G. Effects of light and electron beam irradiation on halide perovskites and their solar cells. *Acc. Chem. Res.* **2016**, *49*, 347−354.
(70) Deretzis, I.; Alberti, A.; Pellegrino, G.; Smecca, E.; Giannazzo, F.; Sakai, N.; Miyasaka, T.; La Magna, A. Atomistic origins of $CH_3NH_3PbI_3$ degradation to PbI_2 in vacuum. *Appl. Phys. Lett.* **2015**, *106*, 131904.
(71) Zhang, L.; Sit, P. H.-L. Ab initio study of interaction of water, hydroxyl radicals, and hydroxide ions with $CH_3NH_3PbI_3$ and $CH_3NH_3PbBr_3$ surfaces. *J. Phys. Chem. C* **2015**, *119*, 22370−22378.
(72) Bryant, D.; Aristidou, N.; Pont, S.; Sanchez-Molina, I.; Chotchunangatchaval, T.; Wheeler, S.; Durrant, J. R.; Haque, S. A. Light and oxygen induced degradation limits the operational stability of methylammonium lead triiodide perovskite solar cells. *Energy Environ. Sci.* **2016**, *9*, 1655−1660.
(73) Su, L.; Lu, G.; Kenens, B.; Rocha, S.; Fron, E.; Yuan, H.; Chen, C.; Van Dorpe, P.; Roeffaers, M. B. J.; Mizuno, H.; Hofkens, J.; Hutchison, J. A.; Uji-i, H. Visualization of molecular fluorescence point spread functions via remote excitation switching fluorescence microscopy. *Nat. Commun.* **2015**, *6*, 6287.
(74) Su, L.; Yuan, H.; Lu, G.; Rocha, S.; Orrit, M.; Hofkens, J.; Uji-i, H. Super-resolution localization and defocused fluorescence microscopy on resonantly coupled single-molecule, single-nanorod hybrids. *ACS Nano* **2016**, *10*, 2455−2466.

DOI: 10.1021/acsomega.6b00107
ACS Omega 2016, 1, 148−159